INORGANIC CHEMISTRY
FRONTIERS

RESEARCH ARTICLE

View Article Online
View Journal | View Issue



Cite this: *Inorg. Chem. Front.*, 2023, **10**, 6622

# Developing a gradient titanium dioxide/amorphous tantalum nitride electron transporting layer for efficient and stable perovskite solar cells†

Yue Gou,[a] Haoyan Wang,[a] Yutao Li,[a] Chenyu Zhao,[a] Lin Fan,[a,b] Maobin Wei,[a,b] Huilian Liu,[a,b] Jinghai Yang,[a,b] Fengyou Wang *[a,b] and Lili Yang *[a,b]

Metal oxides are extensively applied as one of the most potential electron transport layers (ETLs) in perovskite solar cells (PSCs). However, their inherent surface oxygen vacancies and imperfect energy level alignment with the perovskite layer usually result in photogenerated charge recombination at the ETL/perovskite heterointerface. Managing the interface defects and band alignment is significant to decrease energy loss and improve the power conversion efficiency of PSCs. Herein, we develop a gradient $TiO_2$/a-$TaN_x$ (TOAN) ETL, which not only eliminates interfacial defects and improves the crystallization of perovskite films, but also displays good energy level alignment and charge transport characteristics. The $MAPbI_3$ solar cells based on TOAN ETLs achieve an efficiency of 21.41% with an open-circuit voltage of 1.20 V and a short-circuit current density of 22.87 mA $cm^{-2}$. In addition, the device with a TOAN ETL maintains 95% initial efficiency after 30 days in $N_2$ without encapsulation and retains 91% of its initial efficiency after storing for 30 days in an atmospheric environment. This result demonstrates the effectiveness of an inorganic metal nitride as an interface modification layer and provides a reference for the further development of metal nitride electron transport layers.

Received 25th June 2023,
Accepted 13th September 2023

DOI: 10.1039/d3qi01178j

rsc.li/frontiers-inorganic



## Introduction

Organic–inorganic halide perovskite solar cells (PSCs) have rapidly evolved over the past few decades as a promising next-generation photovoltaic technology, owing to their benefits including small exciton binding energy, long carrier diffusion length, high absorption coefficient, ambipolar charge transport, and strong defect tolerance.[1–5] The power conversion efficiency (PCE) of PSCs has risen from 3.8% (in 2009) to 26.1% (certified in 2023) *via* the strategies of thin film crystallization regulation, interface engineering, effective light management, and so on.[6–12]

The electron transfer layer (ETL)/perovskite interface of PSCs plays a key role in tuning the crystallinity of the perovskite layer and promoting the overall charge transport efficiency.[13,14] However, the widely used metal oxide ETLs often have surface oxygen vacancies and undesirable conduction band offsets with the perovskite, resulting in interfacial charge recombination loss. Meanwhile, the hydroxyl group introduced during the ETL fabrication process is easily absorbed into the surface oxygen vacancies, which may trigger the deprotonation reaction with the perovskite layer and degrade the long-term stability of the device. Many strategies are proposed to eliminate the oxygen vacancies and rearrange the energy levels at the ETL/perovskite interface for achieving better cell performance and stability. For instance, several electron-donor groups such as amino (–$NH_2$), carboxyl (–COOH), and carbon–oxygen double bonds (C═O) have been utilized to reduce the uncoordinated dangling bonds at the ETL/perovskite interface,[15–17] which inhibit the non-radiative recombination and cation migration, improving the PCE and retarding the decomposition of the devices. Notably, Sonmezoglu *et al.* adopted a series of modifiers, including 2-methylbenzimidazole, acetylacetone, biopolymer Caf1, and DNA molecules, to modify the ETL surface. These modifiers suppressed the interface-dependent nonradiative recombination and aligned the interface energy levels, leading to a remarkable improvement of the solar cells.[18–21] Furthermore, a common method to strengthen the charge transfer at the ETL/perovskite interface is adjusting the energy level alignment, which could enhance the PCE by reducing the energy loss.[22–24] For example, doping with metals ions, such as lithium, sodium, potassium, and tungsten, can change the bandgap alignment of ETL/perovskite,[25,26] thus improving the conductivity and short-

[a]*Key Laboratory of Functional Materials Physics and Chemistry of the Ministry of Education, Jilin Normal University, Changchun 130103, China.*
*E-mail: wfy@jlnu.edu.cn, llyang1980@163.com*
[b]*National Demonstration Center for Experimental Physics Education, Jilin Normal University, Siping 136000, China*

† Electronic supplementary information (ESI) available. See DOI: https://doi.org/10.1039/d3qi01178j

circuit current ($J_{sc}$) of the devices. The interfacial bandgap alignment can also be adjusted by constructing hybrid ETLs. Chen *et al.* developed a $SnO_2$/2D-$Bi_2O_2Se$ hybrid electron transporting layer, which possesses a better cascade band alignment with the perovskite layer compared to a single $SnO_2$, resulting in low-hysteresis and high-performance PSCs.[27] Zhang *et al.* strengthened the $SnO_2$–perovskite buried interface by a strategy involving pre-grafted halides to manipulate perovskite defects and carrier dynamics, thereby resulting in both favorable perovskite crystallization and minimized interfacial carrier losses.[28] Ghosh *et al.* demonstrated a low temperature solution-processed $TiO_2$/AZO bilayer thin film as an ETL in a planar PSC configuration. The corresponding efficiency is improved owing to the reduction of trap-assisted recombination at the interface and better energy level alignment.[29] Previously, we used an a-$WO_x$/$SnO_2$ ETL to adjust the energy level of the ETL/perovskite interface, which improves the free energy of the ETL/perovskite interface from 0.34 to 0.6 eV and enhances the driving force of charge transfer, yielding a PCE of 20.52%.[30] All the above interface modulators contribute to the development of PSCs from different aspects, but some shortcomings are gradually exposed along with thorough research. For example, the organic modulators are usually subjected to solvent erosion from perovskite precursors and face the thermal instability issue, destroying the interface connection; moreover, the inorganic modulators are more stable but have no ideal passivation capability due to the lack of functionalized groups. Exploring a stable material that can not only reduce interface defects but also accelerate charge extraction at the ETL/perovskite interface is very significant for raising the PSC efficiency.

Transition metal nitrides, as stable inorganic compounds,[31] with abundant N atoms and a tunable bandgap, may satisfy the above requirements simultaneously by donating lone pair electrons as well as forming gradient energy alignment with the perovskite layer. Herein, we developed a gradient titanium dioxide/amorphous tantalum nitride ($TiO_2$/a-$TaN_x$, TOAN) hybrid ETL to suppress ETL/perovskite interfacial energy loss and improve the photovoltaic performance of the PSCs. The TOAN possesses higher conductivity and a more suitable interface energy-level cascade compared to traditional $TiO_2$which contributes to reducing the ETL/perovskite interfacial charge accumulation and the electron transfer barrier. Meanwhile, the N-rich surface of the TOAN ETL can eliminate the ETL/perovskite interfacial defects by forming N–Pb electron transfer channels with the perovskite layer, thus decreasing the non-radiative recombination loss. Concomitantly, the Gibbs free energy of the TOAN substrate is elevated compared with that of the $TiO_2$ ETL, promoting the crystallization and growth of perovskite films. Pinhole-free and compact perovskite films could enhance the environmental stability and photostability of the devices. Consequently, the PSC based on a TOAN ETL showed a higher PCE of 21.47% with negligible hysteresis compared with the $TiO_2$ device that had a PCE of 19.42%. In addition, the PSC based on the TOAN ETL retained 91% of its original efficiency after aging for 30 days under an ambient atmosphere.

## Results and discussion

An ~80 nm tantalum nitride film was prepared at room temperature by radio-frequency magnetron sputtering. Transmission electron microscopy (TEM) and X-ray diffraction (XRD) were conducted to explore the film microstructure. The TEM image shows no microcrystallite, and the diffusion rings are weak and broad, implying the characteristics of an amorphous metallic compound (Fig. S1†).[32] Meanwhile, we only find a wide and degenerated peak of glass at 24.42° from the XRD patterns, which further proves the amorphous nature of the $TaN_x$ (a-$TaN_x$) (Fig. 1a). To study the surface chemical states of a-$TaN_x$ film, X-ray photoelectron spectroscopy (XPS) was performed. The Ta 4f peak can be divided into three doublets, belonging to the Ta $4f_{7/2}$ (24.7, 25.5, and 26.2 eV) and the Ta $4f_{5/2}$ (26.5, 27.4, and 28.2 eV) orbits (Fig. 1b). The dominant Ta $4f_{7/2}$ peak and Ta $4f_{5/2}$ peak at binding energies of 24.7 and 26.5 eV are associated with Ta–N bonding, respectively. The Ta $4f_{7/2}$ and Ta $4f_{5/2}$ subcomponents centered at 25.5 and 27.4 eV are attributed to the Ta-ON species, and the remaining pair of peaks at 26.2 and 28.2 eV represents the Ta–O.[33] These different chemical bonds and valence states of Ta imply that the a-$TaN_x$ films are non-stoichiometric. The reason for the formation of amorphous and non-stoichiometric $TaN_x$ films is that the sputtered $TaN_x$ precursor radicals have a low migration energy on the room-temperature substrate, making them only able to stay in the position where they hit the substrate and leading to a disordered network matrix. Moreover, XPS shows that the atomic ratio of Ta–N is 1 : 2.5, which is higher than the usual 1 : 0.5 and 1 : 1.6 (Fig. 1c).[34,35] This N-rich surface is beneficial to eliminate the trap states at the ETL/perovskite interface and will be discussed later.

We then constructed the $TiO_2$/a-$TaN_x$ (TOAN) film by depositing 5 nm a-$TaN_x$ on the $TiO_2$ surface. The uniform distribution of Ta and N elements indicates that the a-$TaN_x$ is finely distributed on the $TiO_2$ surface (Fig. S2†). The surface morphologies of $TiO_2$ and TOAN films were studied by scanning electron microscopy (SEM, Fig. 1d and e) and atomic force microscopy (AFM, Fig. S3†). The images show that the TOAN film is slightly smoother than the $TiO_2$ film, with the root-mean-square (RMS) roughness reduced from 23.4 nm to 21.7 nm. In addition, since the Ta of a-$TaN_x$ has many more valence electrons compared with the Ti of $TiO_2$, Ta has extra electronic donor centers, which may lead to higher conductivity of TOAN.[36] The electrical properties of $TiO_2$ and TOAN films were characterized in the dark using the vertical current density–voltage ($J$–$V$) test with an FTO/$TiO_2$ (or TOAN)/Ag structure. As shown in Fig. S4,† the increased slope of the TOAN films shows that the resistance values are reduced compared with those of $TiO_2$ for a similar thickness. The conductivity of the films can be calculated using the following equation: $\sigma = d/(AR)$, where $\sigma$ is the conductivity, $A$ is the active area (0.09 $cm^2$), $R$ is the resistance calculated from the dark $I$–$V$ curves, and $d$ is the thickness of the films (~200 nm).[37] The values of $\sigma$ are ~$1.2 \times 10^{-2}$ mS $cm^{-1}$, ~$2.04 \times 10^{-2}$ mS $cm^{-1}$ and ~$3.8 \times 10^{-2}$ mS $cm^{-1}$ for $TiO_2$, TOAN and a-$TaN_x$ films, respectively, which

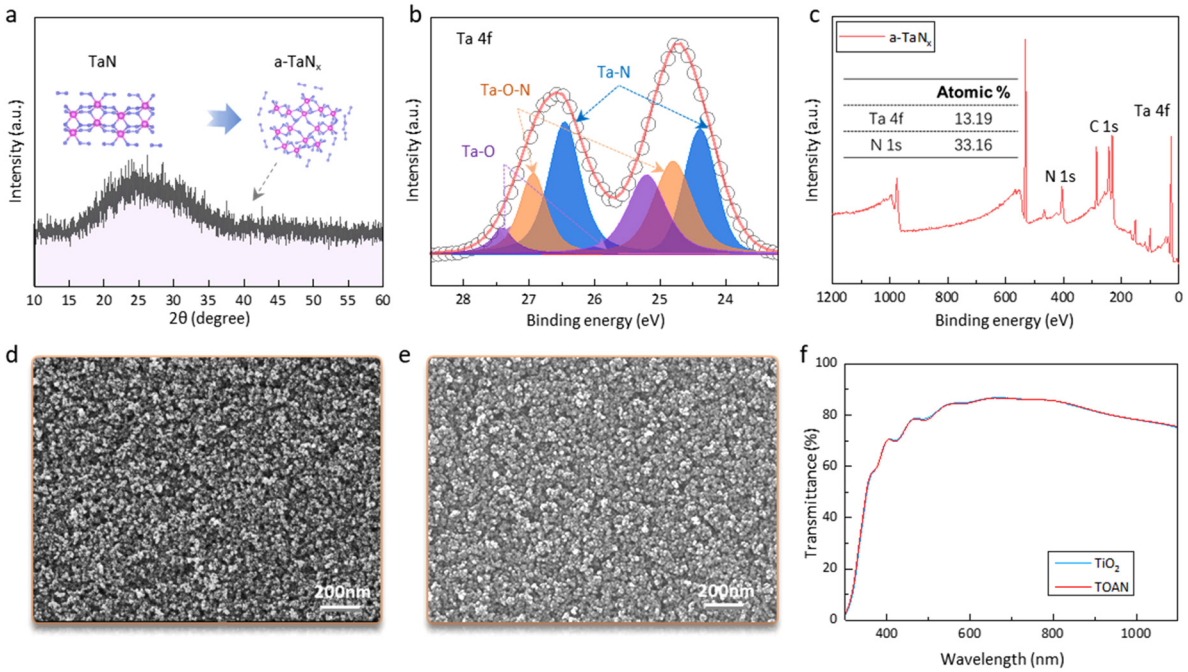


**Fig. 1** Construction and characterization of the TOAN ETL. (a) XRD pattern of the ~80 nm a-$TaN_x$ film deposited on glass. XPS patterns of (b) Ta 4f and (c) a-$TaN_x$ films. The SEM images of (d) $TiO_2$ and (e) TOAN layers on FTO substrates. (f) The optical transmittance of the TiO2 and TOAN layers.

show that the TOAN film has a better charge transport capability than the $TiO_2$ film. Besides that, the efficiency of PSCs is affected by the generation of photogenerated carriers, which is associated with the ETL optical properties. Fig. 1f shows the optical transmittance spectra of $TiO_2$ and TOAN films, both of which exhibit high transmittance in the visible region. The high conductivity, together with the excellent optical transmittance, makes the TOAN a suitable material for thin-film photovoltaic devices.

Ultraviolet–visible (UV–vis) spectroscopy was performed to further study the optical absorption of perovskite films grown on different substrates. Fig. 2a shows that the optical absorption of the two perovskite films is analogous, indicating that the TOAN layer has no additional parasitic absorption, which matches the results in Fig. 1f. The perovskite crystallization is also a key factor influencing the photovoltaic performance of PSCs. Fig. 2b and Fig. S5† present the SEM and AFM images of perovskite films based on $TiO_2$ ($TiO_2$-perovskite) and TOAN (TOAN-perovskite). Interestingly, the TOAN-perovskite shows a uniform surface and lower roughness in contrast to the $TiO_2$-perovskite. Fig. S6† shows that TOAN-perovskite possesses a larger grain size (~800 nm) than $TiO_2$-perovskite (~450 nm). The X-ray diffraction (XRD) peak of TOAN-perovskite is stronger and sharper than that of $TiO_2$-perovskite, and the corresponding full width at half-maximum (FWHM) reduces from 0.228° to 0.182° at the main (110) crystallographic plane, consistent with the increased grain size shown by SEM (Fig. 2c). The favorable crystallization of perovskite films can help reduce their bulk defects. We then measured the Urbach tail energy ($E_u$) of the two perovskite films. A reduced $E_u$ of the TOAN-perovskite film is shown in Fig. 2d, indicating a smaller energetic disorder within the bulk of the film.[38] In order to quantitatively clarify the defect density of the perovskite films, the space-charge limited current (SCLC) was assessed with the device structure FTO/$TiO_2$ (or TOAN)/perovskite/PCBM/Ag (Fig. 2e). The defect density can be calculated using the following equation: $N_{trap} = (2\varepsilon\varepsilon_0 V_{TFL})/(eL^2)$, where $\varepsilon$ is the $MAPbI_3$ permittivity ($\varepsilon$ = 32 F $cm^{-1}$), $\varepsilon_0$ is the vacuum permittivity, $V_{TFL}$ is the trap-filled voltage, $e$ is the unit charge, and $L$ is the thickness of the perovskite.[39] As expected, compared with the $TiO_2$ device ($V_{TFL}$ = 0.89 V, $N_{trap}$ = 2.57 × $10^{16}$ $cm^{-3}$), the TOAN device shows smaller $V_{TFL}$ (0.33 V) and $N_{trap}$ (8.8 × $10^{15}$ $cm^{-3}$). Moreover, as shown in Fig. 2f, the photovoltage decay lifetime of TOAN-perovskite (104 μs) is also higher than that of $TiO_2$-perovskite (32 μs), confirming a decreased non-radiative recombination at the ETL/perovskite interface.[40]

Considering that the preparation process of all of the perovskite films is identical, we deduce that the enhanced crystallization of the perovskite is probably correlated with the surface properties of the substrate. Generally, perovskite nucleation and growth largely depend on the Gibbs free energy ($\Delta G$) of the substrate surface, and the heterogeneous nucleation barrier $\Delta G_{he}$ can be represented by the following equation:[41]

$$\Delta G_{he} = \Delta G_{h0} \cdot f(\theta) \quad (1)$$

$$f(\theta) = \frac{2 - 3\cos\theta + (\cos\theta)^3}{4} \quad (2)$$

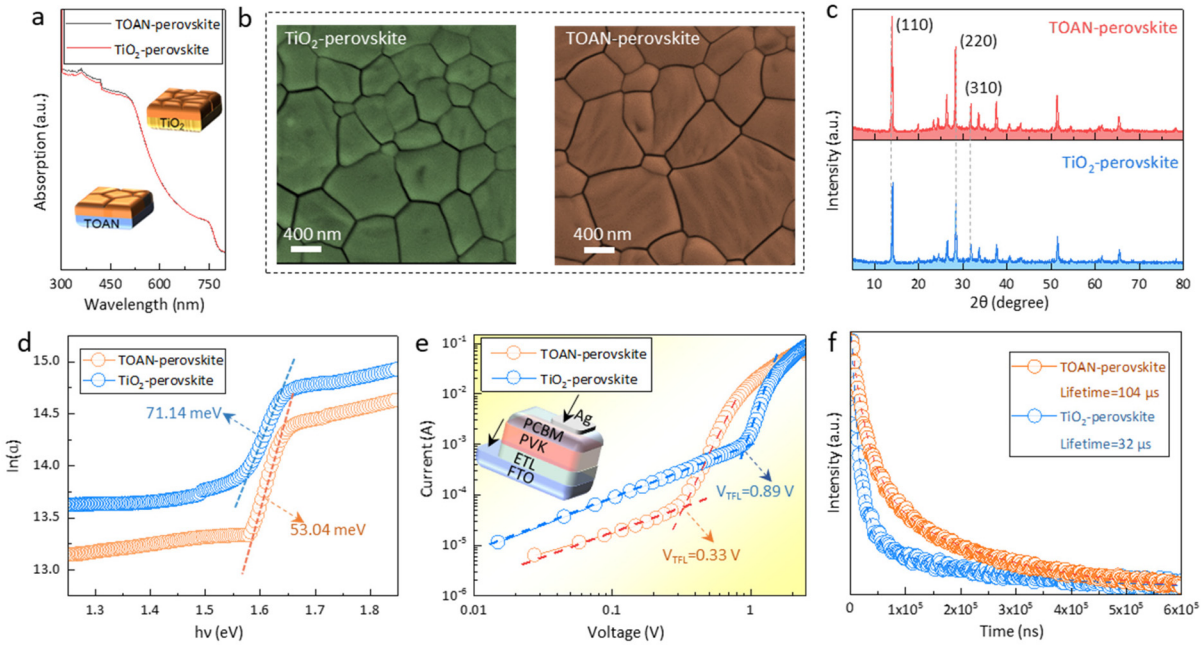


**Fig. 2** Perovskite films grown on $TiO_2$ and TOAN substrates. (a) The UV-vis absorption patterns of the perovskite films grown on $TiO_2$ and TOAN layers. (b) SEM images and (c) XRD patterns of the $TiO_2$- and TOAN-perovskite, respectively. (d) The *hv versus* ln($\alpha$) for the $TiO_2$- and TOAN-perovskite films. The $E_u$ can be obtained from the following equation: $\alpha = \alpha_0 \exp(E/E_u)$, where $\alpha_0$ is a constant. (e) The SCLC curves of the $TiO_2$- and TOAN-devices; the inset exhibits the device structure. (f) Transient photovoltage decay curves for the $TiO_2$- and TOAN-perovskite films.

where $\Delta G_{ho}$ is the Gibbs free energy of homogeneous nucleation and $\theta$ is the contact angle of the precursor solution. According to eqn (1), $\Delta G_{he}$ is related to $\Delta G_{ho}$ and $f(\theta)$. $\Delta G_{ho}$ is invariant in this study since the components of the perovskite precursor have not changed.[42] Consequently, we could conclude that $\Delta G_{he}$ is positively correlated with $f(\theta)$. Fig. 3a shows that the contact angles of the precursor solution on $TiO_2$ and TOAN surfaces are 46° and 69°, respectively, yielding the corresponding $f(\theta)$ values of 0.06 and 0.24, respectively. A small $f(\theta)$ results in a low $\Delta G_{he}$, which contributes to the heterogeneous nucleation process, and thus numerous nuclei are formed, but with smaller grains. Conversely, a larger $f(\theta)$ means a higher $\Delta G_{he}$, which could reduce the nucleation density and leave more space for grain expansion (Fig. 3b). Therefore, the perovskite film based on TOAN possesses larger grain size than the $TiO_2$ counterpart.

The change in $\Delta G_{he}$ may be attributed to the difference in dangling bonds on the substrate surface.[43] Fig. 3c shows that the $TiO_2$ film has three O 1s peaks at 529.79, 531.18, and 531.9 eV, which belong to the lattice oxygen, oxygen deficiency, and O–H bonding, respectively.[44] However, for the TOAN film, the O 1s peak of the oxygen deficiency is apparently weakened, suggesting that the oxygen deficiency defects are passivated by the surface N atoms. We have conducted electron spin resonance (EPR) measurements on both the $TiO_2$ and TOAN films (Fig. S7†). The *g*-value calculated from the resonance magnetic field is 2.006, which is similar to the *g*-value of the free electron (2.008) that corresponds to an oxygen vacancy. The higher peak intensity observed in the TOAN film compared to that in the $TiO_2$ film indicates that the oxygen vacancies on the $TiO_2$ surface are effectively passivated by the a-$TaN_x$ layer.[45–47] This result demonstrates that the redistribution of surface bonds affects the electron configuration of the substrate surface, thereby changing the $\Delta G_{he}$ and the substrate wettability.[48]

Apart from modulating perovskite crystallization, the N-rich surface of the TOAN may also passivate the uncoordinated $Pb^{2+}$ at the perovskite buried interface, reducing the interfacial recombination loss. Fourier transform infrared (FTIR) spectra show that the stretching vibration of the N–H bond in the $TiO_2$-perovskite located at 1499 and 3492 $cm^{-1}$ is obviously shifted to 1491 and 3468 $cm^{-1}$ for the TOAN-perovskite (Fig. S8†). XPS was also conducted for the TOAN-perovskite and $TiO_2$-perovskite. In order to accurately reflect the bonding situation at the ETL/perovskite interface, ion beams were utilized to etch the perovskite films (from the top surface) to ~10 nm before the measurement (Fig. 3d). The Pb $4f_{7/2}$ and Pb $4f_{5/2}$ peaks of the TOAN-perovskite film show a large shift towards lower binding energies compared to those of the $TiO_2$-perovskite. This downshift in peaks in the TOAN-perovskite implies Pb–N coordination between TOAN and perovskite because N can donate electrons to $Pb^{2+}$ dangling bonds, weakening the binding energy of electrons outside the Pb nucleus.[49,50] Therefore, from the overall analysis of the bonding situation, it can be seen that the N in TOAN can not only effectively eliminate the oxygen vacancy defects on the ETL surface, but also passivate the dangling bonds of the perovskite buried interface, polishing the microstructure of the ETL/perovskite interface (Fig. 3e).

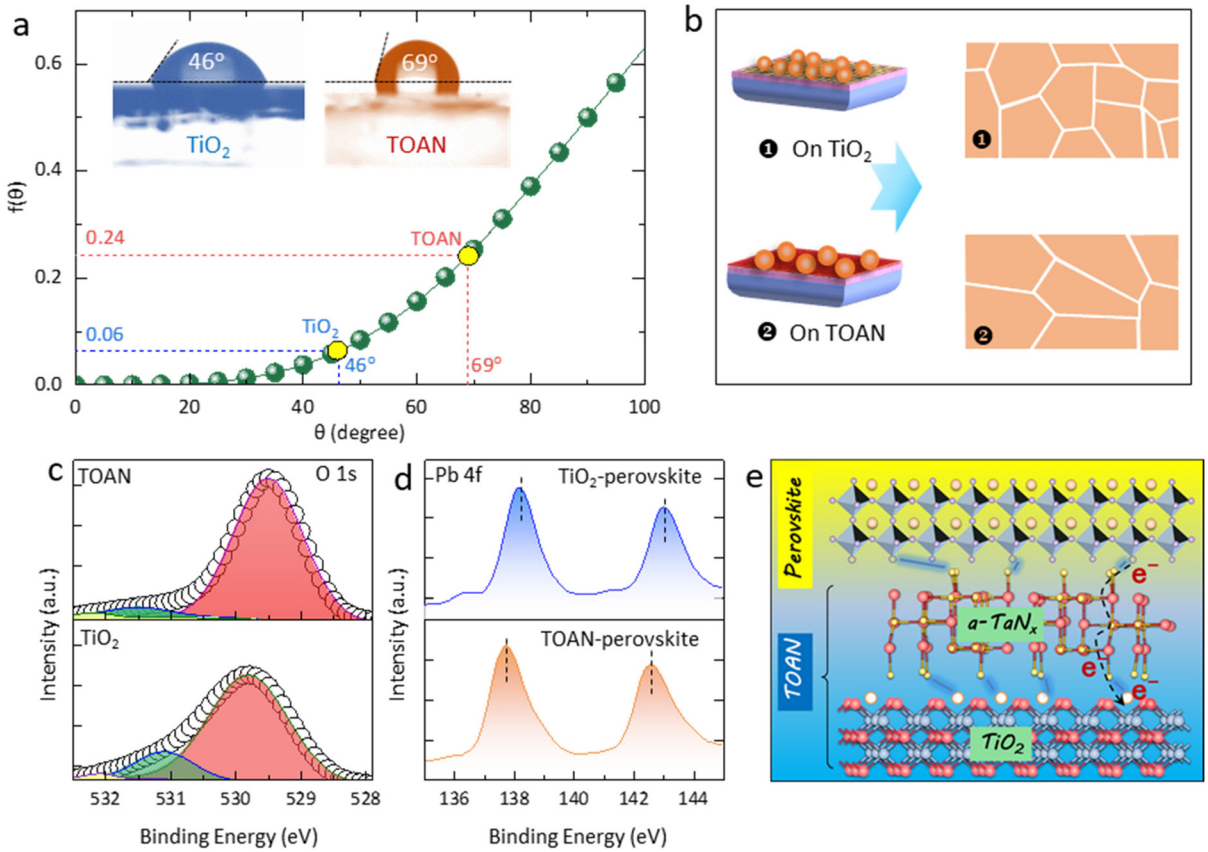


**Fig. 3** The TOAN/perovskite interface. (a) Comparison of the $f(\theta)$ values for $TiO_2$-perovskite and TOAN-perovskite. Inset: the $\theta$ of the perovskite precursors on $TiO_2$ and TOAN substrates. (b) Mechanism diagram of perovskite nucleation on the $TiO_2$ and TOAN substrates, respectively. The XPS patterns for the (c) O 1s and (d) Pb 4f peaks. (e) Schematic of defect reduction at the TOAN/perovskite interface.

The dynamics of charge transfer at the ETL/perovskite interface was measured and is shown in Fig. 4a and b. The photoluminescence (PL) intensity of the TOAN-perovskite film was suppressed compared with that of the $TiO_2$-perovskite film, which is attributed to the more efficient extraction of photogenerated charges from the perovskite to the TOAN layer. The time-resolved PL (TRPL) shows that the decay time of the TOAN-perovskite film is smaller than that of the $TiO_2$-perovskite film (Table S1†), implying that the TOAN film accelerates the charge extraction at the ETL/perovskite interface. The rapid transfer of charges is closely linked with the improved contact properties and the well-matched energy level at the ETL/perovskite interface. We explored the band alignment between the different ETLs and the perovskite layer by UV-vis absorption spectroscopy and ultraviolet photoelectron spectroscopy (UPS). The bandgaps of a-$TaN_x$ and $TiO_2$ calculated by UV-vis absorption spectroscopy are 2.93 and 3.15 eV, respectively (Fig. S9†). The calculated conduction band minima are −4.14 eV for a-$TaN_x$ and −4.25 eV for $TiO_2$ (Fig. 4c and d). Therefore, we can conclude that the TOAN can establish a gradient energy level arrangement with the perovskite photo-absorber layer, promoting charge transport and maintaining a high built-in field for PSCs (Fig. S10†).

Devices with a structure of FTO/$TiO_2$ (or TOAN)/perovskite/spiro-OMeTAD/Ag were fabricated. The cross-sectional SEM image and the structure diagram of the complete device are shown in Fig. 5a and b. Fig. 5c shows the reverse and forward $J$–$V$ curves of the $TiO_2$- and TOAN-PSCs. The TOAN device displays an open circuit voltage ($V_{oc}$) of 1.20 V, a short-circuit current density ($J_{sc}$) of 22.87 mA $cm^{-2}$, a fill factor (FF) of 78.03%, and a champion PCE of 21.41%. In contrast, the device based on the $TiO_2$ ETL yields a $V_{oc}$ of 1.14 V, a $J_{sc}$ of 21.75 mA $cm^{-2}$, an FF of 76.74%, and a PCE of 19.02%. The detailed photovoltaic parameters are summarized in Table S2.† The credibility of $J_{sc}$ was confirmed by external quantum efficiency (EQE) tests (Fig. 5d). The integrated $J_{sc}$ values (21.77 mA $cm^{-2}$ for the TOAN device and 19.61 mA $cm^{-2}$ for the $TiO_2$ device) obtained from EQE curves were found to exhibit the same trend as the $J_{sc}$ values gained from the $J$–$V$ measurement. The output photocurrent is also taken from the maximum power point of the champion devices (Fig. 5e). The TOAN device shows a higher current density and a smaller attenuation compared with the $TiO_2$ device. The stabilized PCE at the maximum power point voltage ($V_{mpp}$) of the champion PSCs was also tested. The TOAN device achieved a steady-state PCE of 19.88% at a $V_{mpp}$ of 1.02 V, whereas the

 

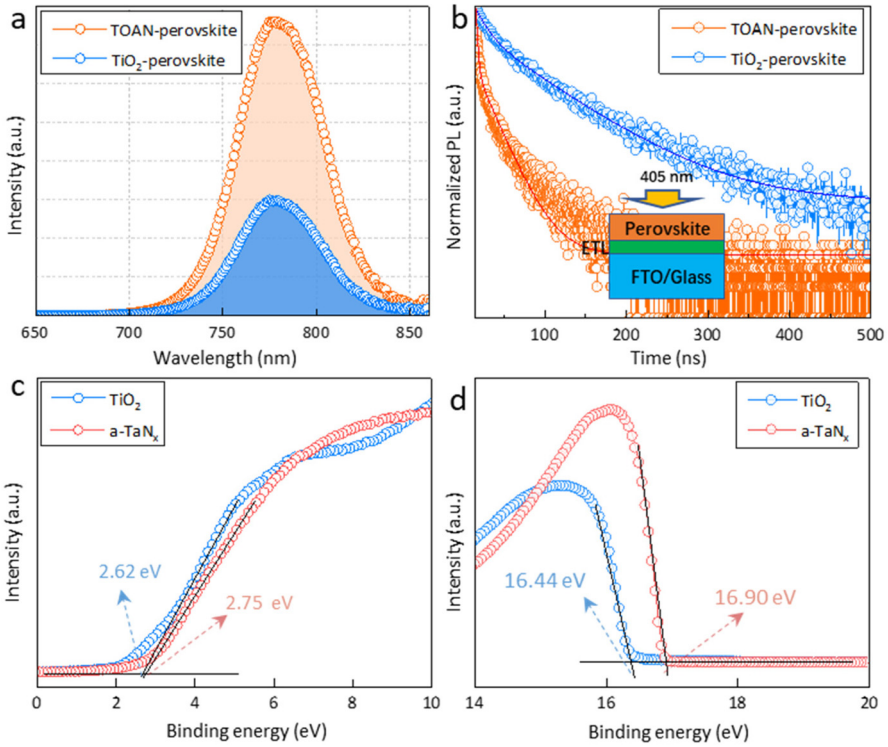


**Fig. 4** Carrier transport at the TOAN/perovskite interface. (a) Steady-state PL and (b) TRPL spectra of the $TiO_2$- and TOAN-perovskite films, respectively. (c) The onset and (d) the cutoff of the UPS spectra for the $TiO_2$ and a-$TaN_x$ films, respectively.

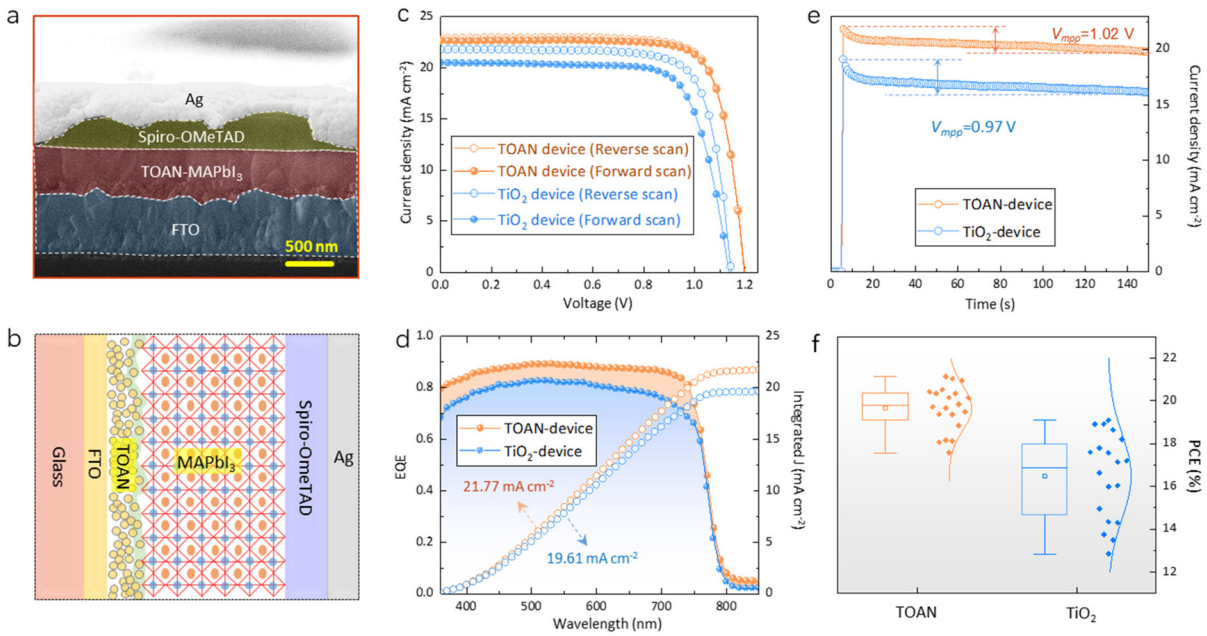


**Fig. 5** Device performance. (a) Cross-sectional SEM and (b) schematic structure of the PSCs. (c) *J*–*V* curves and (d) EQE spectra of the champion $TiO_2$ and TOAN devices. (e) The output photocurrent is taken from the maximum power point of the champion devices. (f) PCE distribution of 20 $TiO_2$ and 20 TOAN devices, respectively.

$TiO_2$ device reached 16.05% at 0.97 V. The statistical distributions of 20 $TiO_2$ and 20 TOAN devices are shown in Fig. 5f (Tables S3 and S4†), which shows that the TOAN devices have a tighter distribution with better repeatability than the $TiO_2$ devices. We also analyzed the reasons and physical mechanisms behind the device performance improvement. The

improvement of $J_{sc}$ can be attributed to the enhanced ETL/perovskite interface charge transfer. Also, the high electrical conductivity of a-$TaN_x$ facilitates efficient electron transfer from the perovskite layer to the ETL, thereby increasing $J_{sc}$. With regard to $V_{oc}$, the use of TOAN as the ETL contributes to a reduction in interface defects between the $TiO_2$ and perovskite layers. By minimizing the energy barriers and charge trapping sites at this interface, TOAN promotes more effective charge separation and reduces non-radiative recombination, resulting in an enhanced $V_{oc}$. TOAN assists in improving the FF of the device because the superior electrical conductivity of TOAN helps reduce charge accumulation and resistive losses within the device, leading to improved charge extraction and reduced series resistance. These factors collectively contribute to improving the charge collection efficiency, leading to a reduction in hysteresis behavior.

The built-in potential ($V_{bi}$) of both cells was studied using capacitance–voltage ($C$–$V$) measurements to analyze the possible mechanism for the improvement in $V_{oc}$ (Fig. S11†). The TOAN device has a larger $V_{bi}$ (1.08 V) than the $TiO_2$ device ($V_{bi}$ = 1.02 V). A higher $V_{bi}$ of the TOAN device indicates a stronger electric field in PSCs, which contributes to the charge separation and collection, thus enabling a larger $V_{oc}$.[51] Meanwhile, the relationship between light intensity and $V_{oc}$ was studied to illustrate the enhancement of the FF. The slope of the fitting line was minimized from $1.53kT/q$ for the $TiO_2$ device to $1.37kT/q$ for the TOAN device, which implies that the trap-assisted surface recombination obviously decreased in the TOAN device (Fig. S12†).[52] We further performed electrochemical impedance spectroscopy (EIS) for both devices to investigate the charge-transfer dynamics under dark conditions. The TOAN device holds a smaller transport resistance ($R_{tr}$, high-frequency component) and a larger recombination resistance ($R_{rec}$, low-frequency component) than the $TiO_2$ device, which demonstrates that the carrier extraction and transport at the interface are enhanced while the interfacial recombination is suppressed by applying the TOAN ETL (Fig. S13†).[53,54] Furthermore, the capacitance–frequency ($C$–$f$) curves of PSCs were drawn to evaluate the defect-induced capacitance value. Fig. S14† shows that the TOAN device has smaller values in the low-frequency region, which means a lower series resistance at the TOAN/perovskite interface than that at the $TiO_2$/perovskite interface, consistent with the reduced interface defects.[55] Therefore, as shown in Fig. S15,† the improved performance of the TOAN-based devices can be attributed to two aspects: (1) the N in TOAN reduces the defect density at the ETL/perovskite interface and regulates the crystallization of the perovskite film, thereby ultimately inhibiting the non-radiative recombination of photogenerated charges; and (2) the TOAN device forms a gradient energy alignment at the ETL/perovskite interface, which promotes charge transfer and strengthens the built-in field of the device.

The PSC stability was also assessed at a relative humidity (RH) of ~35% and a temperature of 25 °C (Fig. S16a†). After 30 days of aging, both the $TiO_2$ device and the TOAN device displayed good stability under a nitrogen atmosphere, which could retain 93% and 95% of the initial PCE, respectively. However, for devices in ambient environment, the TOAN cell shows a higher stability than the $TiO_2$ cell. Moreover, we also studied the operational stability of the PSCs under MPP tracking with continuous light irradiation (Fig. S16b†). The control device shows a downward PCE to 51.5% of the initial PCE after being irradiated for 12 h, and the TOAN-based device presents better long-term stability, keeping more than 80.7% of the original PCE after 12 h of irradiation. To figure out the reason for this improved stability, the XRD patterns of $TiO_2$- and TOAN-perovskite films were further recorded (Fig. S17†). We can observe that none of the fresh perovskite films showed the $PbI_2$ peak (Fig. 2c), but after placing in an atmospheric environment for 3 days at a temperature of 25 °C and a humidity of ~42%, the $PbI_2$ phase was observed in the $TiO_2$-perovskite film. Moreover, Fig. S18† shows the UV-vis absorption spectra of the unencapsulated perovskite film deposited on TOAN and $TiO_2$ substrates. After storing for 15 days in the ambient environment with ~42% humidity at room temperature, the aged TOAN-perovskite film closely resembles the pristine TOAN-perovskite film. However, the absorption of the $TiO_2$-perovskite decreases significantly after 15 days of aging under the same conditions, indicating that this film starts to decompose. The improved stability may be related to the favorable crystallization and the ordered structure of perovskite films, which resist the invasion of oxygen and water molecules, delaying the degradation of the devices. In addition, the reduction of dangling bonds could weaken the deprotonation effect at the ETL/perovskite interface, thus stabilizing the structure of perovskite films.

## Conclusion

In summary, we have developed a gradient TOAN ETL for achieving efficient and stable PSCs. TOAN can not only effectively eliminate the oxygen vacancy defects on the ETL surface, but also passivate the dangling bonds of the perovskite buried interface, polishing the microstructure of the ETL/perovskite interface. Moreover, TOAN can form a gradient bandgap alignment with the perovskite, thereby enhancing the built-in field and interfacial charge transfer. These benefits result in a high PCE of 21.41% and negligible hysteresis for $MAPbI_3$ solar cells. Furthermore, the device based on the TOAN ETL retains 91% of its initial PCE after 30 days under an ambient atmosphere. We believe that this work not only presents the potential of an inorganic metal nitride as an interface modification layer for PSCs, but also provides a reference for the further development of metal nitride electron transport layers for other optoelectronic devices.

## Conflicts of interest

There are no conflicts to declare.

 

## Acknowledgements

The authors gratefully acknowledge the support from the National Natural Science Foundation of China (grant no. 62275101, 11904127, 22075101), the Program for the Development of Science and Technology of Jilin Province (item no. YDZJ202201ZYTS300), and the Program for the Science and Technology of Education Department of Jilin Province (item no. JJKH20220440KJ).

## References

1 V. V. Satale, N. Kumar, H. B. Lee, M. M. Ovhal, S. Chowdhury, B. Tyagi, A. Mohamed and J.-W. Kang, Spray-assisted deposition of a $SnO_2$ electron transport bilayer for efficient inkjet-printed perovskite solar cells, *Inorg. Chem. Front.*, 2023, **10**, 3558–3567.
2 W. Cao, Z. Hu, Z. Lin, X. Guo, J. Su, J. Chang and Y. Hao, Defects and doping engineering towards high performance lead-free or lead-less perovskite solar cells, *J. Energy Chem.*, 2022, **68**, 420–438.
3 H. Wu, B. Murti, J. Singh, P.-K. Yang and M.-L. Tsai, Prospects of metal-free perovskites for piezoelectric applications, *Adv. Sci.*, 2022, **9**, 2104703.
4 X. Yang, Q. Li, Y. Zheng, D. Luo, Y. Zhang, Y. Tu, L. Zhao, Y. Wang, F. Xu and Q. Gong, Perovskite hetero-bilayer for efficient charge-transport-layer-free solar cells, *Joule*, 2022, **6**, 1277–1289.
5 L. Kong, X. Zhang, C. Zhang, L. Wang, S. Wang, F. Cao, D. Zhao, A. Rogach and X. Yang, Stability of perovskite light-emitting diodes: existing issues and mitigation strategies related to both material and device aspects, *Adv. Mater.*, 2022, **34**, 2270300.
6 M. Kim, J. Jeong, H. Lu, T. Lee, F. Eickemeyer, Y. Liu, I. Choi, Y. Jo and H.-B. Kim, Conformal quantum dot-$SnO_2$ layers as electron transporters for efficient perovskite solar cells, *Science*, 2022, **375**, 6578.
7 Q. Dou, T. Whatley, T. Syed, W. Wei and H. Wang, Carbon nanomaterials-polymer composites for perovskite solar cells: Preparation, properties and applications, *J. Mater. Chem. A*, 2022, **10**, 19211–19230.
8 T. Zhou, Z. Xu, R. Wang, X. Dong, Q. Fu and Y. Liu, Crystal growth regulation of 2D/3D perovskite films for solar cells with both high efficiency and stability, *Adv. Mater.*, 2022, **34**, 2200705.
9 Best Research-Cell Efficiency Chart, Photovolataic Research NREL, **https://ww.nrel.gov/pv/cell-efficency.html**.
10 F. Berry, R. Mermet-Lyaudoz, J. Davila, D. Djemmah, H. Nguyen, C. Seassal, E. Fourmond, C. Chevalier, M. Amara and E. Drouard, Light management in perovskite photovoltaic solar cells: A perspective, *Adv. Energy Mater.*, 2022, **12**, 2200505.
11 J. Wawrzyniak, K. Grochowska, J. Karczewski, P. Kupracz, J. Ryl, A. Dolega and K. Siuzdak, The geometry of free-standing titania nanotubes as a critical factor controlling their optical and photoelectrochemical performance, *Surf. Coat. Technol.*, 2020, **389**, 125628.
12 Y. Chao, J. Chen, D. Yang, Y. Tseng, C.-H. Hsu and J. Chen, High-performance non-volatile flash photomemory via highly oriented quasi-2D perovskite, *Adv. Funct. Mater.*, 2022, **32**, 2112521.
13 Z. Lin, W. Zhang, Q. Cai, X. Xu, H. Dong, C. Mu and J. Zhang, Precursor engineering of the electron transport layer for application in high-performance perovskite solar cells, *Adv. Sci.*, 2021, **8**, 2102845.
14 H. Wang, Z. Zhang, J. Milic, L. Tan, Z. Wang, R. Chen, X. Jing, C. Yi, Y. Ding and Y. Li, Water stable haloplumbate modulation for efficient and stable hybrid perovskite photovoltaics, *Adv. Energy Mater.*, 2021, **11**, 2101082.
15 B. Chen, H. Chen, Y. Hou, J. Xu, S. Teale, K. Bertens, H. Chen, A. Proppe, Q. Zhou and D. Yu, Passivation of the buried interface via preferential crystallization of 2D perovskite on metal oxide transport layers, *Adv. Mater.*, 2021, **33**, 2103394.
16 W. Pan, J. Lin, J. Wu, B. Rong, X. Zhang, Q. Chen, M. Zhang, S. Wang, W. Sun and X. Wang, Interface modification by formamidine acetate for efficient perovskite solar cells, *Sol. Energy*, 2022, **232**, 304–311.
17 H. Ban, T. Nakajima, Z. Liu, H. Yu, Q. Sun, L. Dai, Y. Shen, X. Zhang, J. Zhu and P. Chen, Over 8% efficient $CsSnI_3$-based mesoporous perovskite solar cells enabled by two-step thermal annealing and surface cationic coordination dual treatment, *J. Mater. Chem. A*, 2022, **10**, 3642–3649.
18 S. Sonmezoglu and S. Akin, Suppression of the interface-dependent nonradiative recombination by using 2-methylbenzimidazole as interlayer for highly efficient and stable perovskite solar cells, *Nano Energy*, 2020, **76**, 105127.
19 H. J. Lee, J. K. Park, J. H. Heo and S. H. Im, Acetylacetone-$TiO_2$ promoted large area compatible cascade electron transport bilayer for efficient perovskite solar cells, *Energy Environ. Mater.*, 2023, e12582.
20 S. Akin, Y. Ulusu, H. Waller, J. H. Lakey and S. Sonmezoglu, Insight into interface engineering at $TiO_2$/Dye through molecularly functionalized Caf1 biopolymer, *ACS Sustainable Chem. Eng.*, 2018, **6**, 1825–1836.
21 Ö. Ateş Sönmezoğlu, S. Akın, B. Terzi, S. Mutlu and S. Sönmezoğlu, An effective approach for high-efficiency photoelectrochemical solar cells by using bifunctional DNA molecules modified photoanode, *Adv. Funct. Mater.*, 2016, **26**, 8776–8783.
22 J. Zhang, J. Fu, Q. Chen, H. Ma, Z. Jiang, Z. Zhang, Y. Zhou and B. Song, 3,5-Difluorophenylboronic acid-modified $SnO_2$ as ETLs for perovskite solar cells: PCE > 22.3%, T-82 > 3000 h, *Chem. Eng. J.*, 2022, **433**, 133744.
23 D. Saranin, S. Pescetelli, A. Pazniak, D. Rossi, A. Liedl, A. Yakusheva, L. Luchnikov, D. Podgorny, P. Gostischev and S. Didenko, Transition metal carbides (MXenes) for efficient NiO-based inverted perovskite solar cells, *Nano Energy*, 2021, **82**, 105771.
24 Q. Guo, J. Wu, Y. Yang, X. Liu, W. Sun, Y. Wei, Z. Lan, J. Lin, M. Huang and H. Chen, Low-temperature processed

rare-earth doped brookite $TiO_2$ scaffold for UV stable, hysteresis-free and high-performance perovskite solar cells, *Nano Energy*, 2020, **77**, 105183.

25 R. Azmi, S. Hwang, W. Yin, T.-W. Kim, T. Ahn and S.-Y. Jang, High efficiency low-temperature processed perovskite solar cells integrated with alkali metal doped ZnO electron transport layers, *ACS Energy Lett.*, 2018, **3**, 1241–1246.

26 H. Wang, C. Zhao, L. Yin, X. Li, X. Tu, E. Lim, Y. Liu and C. Zhao, W-doped $TiO_2$ as electron transport layer for high performance solution-processed perovskite solar cells, *Appl. Surf. Sci.*, 2021, **563**, 150298.

27 J. Chen, J. Zhang, C. Huang, Z. Bi, X. Xu and H. Yu, $SnO_2$/2D-$Bi_2O_2Se$ new hybrid electron transporting layer for efficient and stable perovskite solar cells, *Chem. Eng. J.*, 2021, **410**, 128436.

28 J. Deng, K. Wei, L. Yang, L. Lin, Y. Xiao, X. Cai, C. Zhang, D. Wu, X. Zhang and J. Zhang, Halides-enhanced buried interfaces for stable and extremely low-voltage-deficit perovskite solar cells, *Adv. Mater.*, 2023, **35**, 2300233.

29 N. K. Rana, A. Kumar, N. Chander and D. S. Ghosh, Fabrication of a highly functional $TiO_2$/AZO bilayer electron transport layer for planar perovskite solar cells, *ACS Appl. Electron. Mater.*, 2023, **5**, 1050–1056.

30 F. Wang, Y. Zhang, M. Yang, J. Du, L. Xue, L. Yang, L. Fan, Y. Sui, J. Yang and X. Zhang, Exploring low-temperature processed a-$WO_x$/$SnO_2$ hybrid electron transporting layer for perovskite solar cells with efficiency > 20.5%, *Nano Energy*, 2019, **63**, 103825.

31 K. Chaudhuri, A. Shaltout, D. Shah, U. Guler, A. Dutta, V. Shalaev and A. Boltasseva, Photonic spin Hall effect in robust phase gradient metasurfaces utilizing transition metal nitrides, *ACS Photonics*, 2019, **6**, 99–106.

32 Y. Shen and Y. Mai, Structural studies of amorphous and crystallized tungsten nitride thin films by EFED, XRD and TEM, *Appl. Surf. Sci.*, 2000, **16**, 59–68.

33 X. Yang, E. Aydin, H. Xu, J. Kang, M. Hedhili, W. Liu, Y. Wan, J. Peng, C. Samundsett and A. Cuevas, Tantalum nitride electron-selective contact for crystalline silicon solar cells, *Adv. Energy Mater.*, 2018, **8**, 1800608.

34 H. Jiang, L. Feng, S. Zhu, S. Li and S. Zang, Hydrous $RuO_2$ and $Co_xN_y$ difunction-modified $Ta_3N_5$@$Ta_2N$ multi-heterojunction nanoplates for efficient visible-light-driven photocatalytic hydrogen production, *Int. J. Hydrogen Energy*, 2021, **46**, 39855–39867.

35 C. Wang, T. Hisatomi, T. Minegishi, M. Nakabayashi, N. Shibata, M. Katayama and K. Domen, Effects of interfacial layers on the photoelectrochemical properties of tantalum nitride photoanodes for solar water splitting, *J. Mater. Chem. A*, 2016, **4**, 13837–13843.

36 A. Culu, I. Kaya and S. Sonmezoglu, Spray-pyrolyzed tantalium-doped $TiO_2$ compact electron transport layer for UV-photostable planar perovskite solar cells exceeding 20% efficiency, *ACS Appl. Energy Mater.*, 2022, **5**, 3454–3462.

37 B. Jin, Y. Ming, Z. Wu, J. Cao, Y. Liu, Y. Zhu, S. Wang, Z. Liang and C. Wu, Silk fibroin induced homeotropic alignment of perovskite crystals toward high efficiency and stability, *Nano Energy*, 2022, **94**, 106936.

38 J.-C. Hebig, I. Kuhn, J. Flohre and T. Kirchartz, Optoelectronic properties of $(CH_3NH_3)_3$ $Sb_2I_9$ thin films for photovoltaic applications, *ACS Energy Lett.*, 2016, **1**, 309–314.

39 Y. Yun, D. Vidyasagar, M. Lee, O. Gong, J. Jung, H.-S. Jung, D.-H. Kim and S. Lee, Intermediate phase-free process for methylammonium lead iodide thin film for high-efficiency perovskite solar cells, *Adv. Sci.*, 2021, **8**, 2102492.

40 P. Wang, B. Chen, R. Li, S. Wang, Y. Li, X. Du, Y. Zhao and X. Zhang, 2D perovskite or organic material matter? Targeted growth for efficient perovskite solar cells with efficiency exceeding 24%, *Nano Energy*, 2022, **94**, 106914.

41 B. Fan, J. Xiong, Y. Zhang, C. Gong, F. Li, X. Meng, X. Hu, Z. Yuan, F. Wang and Y. Chen, A bionic interface to suppress the coffee-ring effect for reliable and flexible perovskite modules with a near-90% yield rate, *Adv. Mater.*, 2022, **34**, 2201840.

42 H. Zhao, S. Wang, M. Sun, F. Zhang, X. Li and Y. Xiao, Enhanced stability and optoelectronic properties of $MAPbI_3$ films by a cationic surface-active agent for perovskite solar cells, *J. Mater. Chem. A*, 2018, **6**, 10825–10834.

43 Q. Wang, M. Xue and Z. Zhang, Chemical synthesis of borophene: Progress and prospective, *Acta Phys.-Chim. Sin.*, 2019, **35**, 565–571.

44 Q. Zhou, D. He, Q. Zhuang, B. Liu, R. Li, H. Li, Z. Zhang, H. Yang, P. Zhao and Y. He, Revealing steric-hindrance-dependent buried interface defect passivation mechanism in efficient and stable perovskite solar cells with mitigated tensile stress, *Adv. Funct. Mater.*, 2022, **32**, 2205507.

45 F. Ali, N. D. Pham, H. J. Bradford, N. Khoshsirat, K. Ostrikov, J. M. Bell, H. Wang and T. Tesfamichael, Tuning the amount of oxygen vacancies in sputter-deposited $SnO_x$ films for enhancing the performance of perovskite solar cells, *ChemSusChem*, 2018, **11**, 3096–3103.

46 N. J. Jeon, T. Y. Yang, H. H. Park, J. Seo, D. Y. Nam, D. Jeong, S. Hong, S. H. Kim, J. M. Cho, J. J. Jang and J. K. Lee, Thermally activated, light-induced electron-spin-resonance spin density reflected by photocurrents in a perovskite solar cell, *Appl. Phys. Lett.*, 2019, **114**, 013903.

47 F. Ali, N. D. Pham, L. Fan, V. Tiong, K. Ostrikov, J. M. Bell, H. Wang and T. Tesfamichael, Low hysteresis perovskite solar cells using an electron-beam evaporated $WO_{3-x}$ thin film as the electron transport layer, *ACS Appl. Energy Mater.*, 2019, **2**, 5456–5464.

48 H. Kim, J. Hong, C. Kim, E.-Y. Shin, M. Lee, Y.-Y. Noh, B. Park and I. Hwang, Impact of hydroxyl groups boosting heterogeneous nucleation on perovskite grains and photovoltaic performances, *J. Phys. Chem. C*, 2018, **122**, 16630–16638.

49 S. Zhan, Y. Duan, Z. Liu, L. Yang, K. He, Y. Che, W. Zhao, Y. Han, S. Yang and G. Zhao, Stable 24.29%-efficiency $FA_{0.85}MA_{0.15}PbI_3$ perovskite solar cells enabled by methyl haloacetate–lead dimer complex, *Adv. Energy Mater.*, 2022, **12**, 2200867.

 

50 J. Guo, J. Sun, L. Hu, S. Fang, X. Ling, X. Zhang, Y. Wang, H. Huang, C. Han and C. Cazorla, Indigo: A natural molecular passivator for efficient perovskite solar cells, *Adv. Energy Mater.*, 2022, **12**, 2200537.
51 X. Zhuang, D. Zhou, S. Liu, R. Sun, Z. Shi, L. Liu, T. Wang, B. Liu, D. Liu and H. Song, Learning from plants: Lycopene additive passivation toward efficient and "fresh" perovskite solar cells with oxygen and ultraviolet resistance, *Adv. Energy Mater.*, 2022, **12**, 2200614.
52 A. Wang, X. Deng, J. Wang, S. Wang, X. Niu, F. Hao and L. Ding, Ionic liquid reducing energy loss and stabilizing $CsPbI_2Br$ solar cells, *Nano Energy*, 2021, **81**, 105631.
53 Y. Niu, Y. Peng, X. Zhang, Y. Ren, R. Ghadari, J. Zhu, G. Tulloch, H. Zhang, P. Falaras and L. Hu, Resonant molecular modification for energy level alignment in perovskite solar cells, *ACS Energy Lett.*, 2022, **7**, 3104–3111.
54 Y. Wang, Y. Yang, N. Li, M. Hu, S. Raga, Y. Jiang, C. Wang, X. Zhang, M. Lira-Cantu and F. Huang, Ionic liquid stabilized perovskite solar modules with power conversion efficiency exceeding 20%, *Adv. Funct. Mater.*, 2022, **32**, 2204396.
55 Y. Xiong, L. Xu, P. Wu, L. Sun, G. Xie and B. Hu, Bismuth doping-induced stable Seebeck effect based on $MAPbI_3$ polycrystalline thin films, *Adv. Funct. Mater.*, 2019, **29**, 1900615.